Detection of land surface induced atmospheric water vapor patterns

Tobias Marke[1], Ulrich Löhnert[1], Vera Schemann[1], and Susanne Crewell[1]

[1]Institute for Geophysics and Meteorology, University of Cologne, Germany

Correspondence: Tobias Marke tmarke@meteo.uni-koeln.de

Abstract. Finding observational evidence of land surface atmosphere interactions is crucial for understanding the spatial and temporal evolution of the boundary layer, as well as for model evaluation, in particular large-eddy simulation (LES) models. In this study, the influence of a heterogeneous land surface on the spatial distribution of atmospheric water vapor is assessed. Ground-based remote sensing measurements of a scanning microwave radiometer (MWR) are used in a long-term study over six years to characterize spatial heterogeneities in integrated water vapor (IWV) during clear sky conditions at the Jülich Observatory for Cloud Evolution (JOYCE). The resulting deviations from the mean of the scans reveal a direction-dependent IWV that is visible throughout the day. Comparisons to a satellite derived spatial IWV distribution show a good agreement for a selection of satellite overpasses during convective situations. With the help of a land use type classification and information on the topography, the main type for the regions with a positive IWV deviation was determined to be agricultural fields and nearby open pit mines. Negative deviations occurred mainly above elevated forests and urban areas. In addition, high resolution large-eddy simulations (LES) are used to investigate changes in the water vapor and cloud fields for an altered land use input.

1 Introduction

Interactions between the land surface and the atmospheric boundary layer can have significant influences on the regional weather and climate. Heterogeneity in land use, among other parameters characterized by soil type, vegetation and urban areas, induces spatial variability in surface fluxes of momentum, sensible and latent heat. Numerical studies suggest, that contrasts in land surface fluxes are responsible for mesoscale circulations and considerably affect the state of the atmospheric boundary-layer in a non-linear way (e.g. Ookouchi et al., 1984; Pielke et al., 1991; Clark and Arritt, 1995). On a more local scale the transport of energy and water vapor into the atmosphere can trigger the formation of shallow convective clouds and precipitation (e.g. Rabin et al., 1990; Avissar and Schmidt, 1998). Because this small scale variability can not be resolved by most weather forecast and climate models, it needs to be parameterized. This requires assumptions near the surface boundaries, which strongly affects exchange processes. Unresolved patterns in the models are crucial, since the resulting gradients directly influence the fluxes and hence the evolution of the model state (Simmer et al., 2015). Monitoring and modeling these spatial patterns and interactions is the main focus of this study, which is conducted within the framework of the Transregional Collab-

orative Research Centre 32 (TR32) "Patterns in Soil-Vegetation-Atmosphere Systems" (www.tr32.de). The scope of TR32, as described in Simmer et al. (2015), is to improve the understanding and prediction capabilities of the spatiotemporal evolution of the terrestrial system across scales using measurement techniques and modeling platforms by integrating activities of several research groups.

Since the scales of surface heterogeneity and resulting interaction processes with the overlying boundary-layer are in the order meters to kilometers, a frequently used tool for studying these interaction processes on a local scale is conducting high resolution large-eddy simulations (LES) (e.g. Courault et al., 2007; Huang and Margulis, 2009; Maronga and Raasch, 2013; Shao et al., 2013). By altering the land surface properties, the turbulence resolving simulations provide estimates of the resulting effect on the boundary-layer structure. In this way Vilà-Guerau De Arellano et al. (2014) found differences in cloud dynamics that can be related to the partitioning of the surface fluxes determined by the plant functional type. In van Heerwaarden and Vilà-Guerau De Arellano (2008) an enhancement of cloud formation over heterogeneous landscapes using different Bowen ratios is indicated.

For a better understanding of the influence of the land surface on the atmospheric state and in order to evaluate model findings, ground-based observations by current state-of-the-art remote sensing instrumentation can be used. Significant effects of heterogeneous land use on the turbulent fluxes and connections to clouds have been shown in several field campaigns in a short-term perspective (Weckwerth et al., 2004; Beyrich et al., 2006; Wulfmeyer et al., 2011; Späth et al., 2016; Macke et al., 2017; Wulfmeyer et al., 2018). Investigating the influence of land use heterogeneity on boundary-layer characteristics, such as water vapor and clouds, from long-term measurements can play a key role in finding systematically significant patterns in relations between the local land surface and atmosphere above.

As a key parameter that connects vegetation activity and the boundary-layer, the atmospheric water vapor plays an important role within the hydrological cycle, but also for the energy balance at the surface and within the atmosphere. Späth et al. (2016) investigated water vapor fields for a limited amount of time in a campaign with a scanning differential absorption lidar and found gradients related to surface elevation and land cover type. But also long-term studies of the spatiotemporal variability of water vapor already revealed terrain-related processes in a mountainous area (Adler et al., 2016) by using scans of a passive ground-based microwave radiometer (MWR). Compared to the widely used satellite observations for spatially resolved water vapor estimates, available only for a handful of overpasses per day, the MWR is well suited for continuous and temporally highly resolved measurements at a certain location. While MWR profile measurements of humidity suffer from a coarse resolution, a good agreement between zenith measurements of integrated water vapor (IWV) using MWR, satellite and Global Positioning System (GPS) observations was shown in Steinke et al. (2015). Also, the MWR has already proven to be able to detect horizontal humidity gradients by retrieving IWV values in a scanning configuration (Kneifel et al., 2009; Schween et al., 2011).

To address the question whether spatial water vapor distributions can be connected to land surface properties, this observational and modeling study focuses on the long-term pattern of azimuthal IWV deviations derived from satellite and ground-based measurements at the Jülich ObservatorY of Cloud Evolution (JOYCE, Löhnert et al. (2015)) in Western Germany (50.91°N, 6.41°E). At JOYCE, various remote sensing instruments, including a scanning MWR, are deployed since 2011 to continuously monitor water vapor, clouds and precipitation. For comparing the spatial IWV distribution derived from the MWR with an independent measurement, a satellite water vapor product is used at high spatial resolution. In addition, a Doppler wind lidar is available for a characterization of the atmospheric boundary-layer in terms of the winds and turbulent mixing processes that control the exchange of water vapor between the surface and the atmosphere. The impact of the land surface on the atmospheric water vapor distribution is evaluated by the comparison of the derived IWV deviations to a detailed land use map. To better understand the impact of the land surface on the evolution of the cloudy boundary-layer, sensitivity studies with high resolution LES are performed with different land use type settings.

The details of the utilized instruments and data of this study in Sect. 2 is followed by the description of the data sample derivation used in the long-term analysis. For a better description of the state of the boundary-layer during clear-sky conditions and large scale effects, the results are shown together with wind and turbulence statistics derived from Doppler lidar measurements during the MWR scans and a reanalysis product (Sect. 3.1). Subsequently, the IWV deviations derived from MWR scans and for a collection of satellite overpasses are compared (Sect. 3.2). Also the dependence on wind direction and wind speed is presented together with a single case. A model case study is complemented by the analysis of two large-eddy simulations focusing on the land use influence on the evolution of the cloudy boundary-layer (Sect. 4) and a summary of the results is given in Sect. 5.

2 Instruments and data

2.1 Microwave radiometer

The microwave radiometer HATPRO (Humidity And Temperature PROfiler) at JOYCE utilizes direct detection receivers and measures the brightness temperatures (TB) at 7 channels in the K-band from 22 GHz to 32 GHz and at 7 channels also in the V-band from 52 GHz to 58 GHz. In this study, the observations of the 7 K-band channels with a 1–2 s temporal resolution are taken into account. A statistical approach based on a least squares linear regression model (Löhnert and Crewell, 2003) is applied to derive IWV, absolute humidity (q) and liquid water path (LWP) using observations of the downwelling microwave radiance along the water vapor absorption line between 22.24 and 27.84 GHz and in the atmospheric window at 31.4 GHz. The instrument is capable of observing in high temporal resolutions (Rose et al., 2005) and the absolute error in zenith TB measurements of 0.5 K is mainly determined by the instrument absolute calibration (Maschwitz et al., 2013). This accuracy converts into an uncertainty of 0.5–0.8 $\mathrm{kg\,m^{-2}}$ in the derived IWV and 20–30 $\mathrm{g\,m^{-2}}$ for LWP.

The zenith measurements (IWV_z) alternate with full azimuth scans in $10°$ steps at $30°$ elevation angle. The degrees of freedom for signal (DFS) are usually between 1–2 for MWR humidity retrievals and the highest information content can be found in the boundary-layer. For the zenith retrieval 1.87 DFS and for the $30°$ (slant path) retrieval 2.14 DFS are identified. The scans are available between June 2012–June 2015 and starting from June 2018. In 2016 and 2017 no MWR scans were performed. The scanning frequency is $15\,\mathrm{min}$ and is increased to $10\,\mathrm{min}$ between 25 June and 18 July 2018 and decreased to $30\,\mathrm{min}$ after 18 July 2018. Due to directional dependent interference in the unprotected 26.24 GHz channel, specific azimuth directions are not considered ($50°$, $160°$, $180°$, $260°$). Since the excluded azimuth directions are not connected, no larger gap is apparent and a smooth transitions between the gaps can be assumed. Therefore the missing IWV values are filled using a linear interpolation. For all scans, the derived values for LWP, IWV and q are air-mass corrected to account for the slant angle of the scanning MWR.

2.2 Doppler lidar and boundary-layer classification

As a pulsed lidar system, the Halo Photonics Streamline Doppler lidar (Pearson et al., 2009) provides range-resolved profile measurements of radial Doppler velocity and backscattered signal. With a wavelength of 1.5 μm (near-IR) the instrument is sensitive to the backscatter of aerosols and clouds and is able to scan the full hemisphere. The maximum detectable range depends on the presence of atmospheric particles and the lowest reliable range is at 105 m. At JOYCE the system is set to a range resolution of 30 m and performs plan position indicator scans every 15 min to estimate wind speed and direction profiles based on the velocity-azimuth display (VAD) method using 36 beams at $75°$ elevation. In addition the Doppler beam swing (DBS) technique with three beams and range height indicator scans are scheduled every 5 min and 30 min, respectively. The remaining time, the instrument is staring zenith to derive the vertical velocity with high temporal resolution (1 s).

To study land surface atmosphere exchange processes it is crucial to know the turbulent state of the boundary-layer. Therefore an objective classification of the mixing sources presented by Manninen et al. (2018) is utilized to describe the turbulence characteristics during MWR scans at JOYCE. The method is based on the combination of multiple Doppler lidar quantities including the dissipation rate of turbulent kinetic energy (TKE) derived from vertically pointing observations using the method presented in O'Connor et al. (2010). The TKE dissipation rate is based on the variance of the observed mean Doppler velocity and allows for a threshold based estimation of the convective boundary-layer (CBL) height by determining the last range bin in each profile with significant turbulence in a bottom-up approach.

2.3 MODIS IWV

The passive, imaging Moderate Resolution Imaging Spectroradiometer (MODIS) measures in 36 spectral bands ranging from 0.4 μm to 14.4 μm. Two MODIS instruments are currently airborne on NASA's sun-synchronous near-polar-orbiting Earth Observing System Terra and Aqua satellites. A full coverage of the globe is achieved in 1–2 days with an orbit height of 705 km and a scan rate of 20.3 rpm. The swath dimension of MODIS is 2330 km (cross track) and 10 km (along track at nadir). Within the 36 spectral bands, five channels in the 0.8–1.3 μm near-infrared spectral region can be used for water vapor remote sensing

(Gao and Kaufman, 2003). For IWV estimates the Level-2 (Collection 6.1) near-infrared retrieval (MODIS-NIR) with a 1 km spatial resolution is chosen. The retrieval by Gao and Kaufman (2003) is based on three channels at 0.936 μm, 0.940 μm and 0.905 μm for the water vapor absorption and at 0.865 μm and 1.24 μm to correct for atmospheric gaseous absorption. In order to derive the total vertical amount of water vapor, the reflected NIR solar radiation in the water vapor absorption chan-

5 nel is compared to the window channels yielding the atmospheric water vapor transmittance. The amount of water vapor is then obtained from look-up tables derived from a line-by-line atmospheric transmittance code. Reliable estimates of the water vapor total column amount over land areas can only be inferred during daytime and for cloud free regions. Typical errors of the MODIS-NIR water vapor product range between 5–10%. Here, a height correction similar to Steinke et al. (2015) of the retrieved values is performed due to the variations of the horizontal and height distance to JOYCE per flight track of MODIS.

10 The height difference is corrected by assuming an exponential decrease of the humidity profile and by using the water vapor density obtained from measurements of temperature, humidity and pressure of a weather sensor attached to the MWR and the topography with a 200 m horizontal resolution. Furthermore, the IWV product was resampled to 100 m for calculating the mean values of several overpasses.

15 ## 2.4 ERA5 data products

To distinguish between local influences and large scale features regarding the observed spatial pattern of IWV deviations, the reanalysis products of ERA5 with a 31 km horizontal resolution are analyzed (Copernicus Climate Change Service (C3S), 2017). Besides the u and v wind components at different pressure levels (1000 hPa, 700 hPa), also the direction of the IWV transport (IWVT, in degree) is considered at a 3 h temporal resolution for the closest point to JOYCE. The vertical integral

20 of water vapor flux, used to derive IWVT, is calculated utilizing the specific humidity and winds on model levels. The ERA5 IWV is selected at the closest output time to the MWR scans.

2.5 ICON-LEM

As a state-of-the-art atmospheric modeling system, the ICOsahedral Non-hydrostatic model ICON (Zängl et al., 2015) has been developed by the German Weather Service (DWD) and the Max Planck Institute for Meteorology (MPI-M). The ICON

25 Large-Eddy Model (ICON-LEM) was designed within the framework of the High Definition Clouds and Precipitation for advancing Climate Prediction (HD(CP)[2]) project for improving moist processes in climate prediction models (Heinze et al., 2017). In this study, the ICON-LEM simulations are used to provide a spatial representation of the IWV field to compare with the measurements obtained from the scanning MWR and the MODIS-NIR water vapor product around JOYCE.

30 A good agreement between simulations of ICON-LEM using high grid resolutions of up to 156 m and observations was already shown in Heinze et al. (2017) concerning turbulence, column water vapor and cumulus clouds (compared to satellite observations). Also the topographic influence on the wind field was shown in ICON-LEM simulations and observations at JOYCE (Marke et al., 2018). Therefore a similar setup with a domain radius size of 10 km, 78 m horizontal resolution and
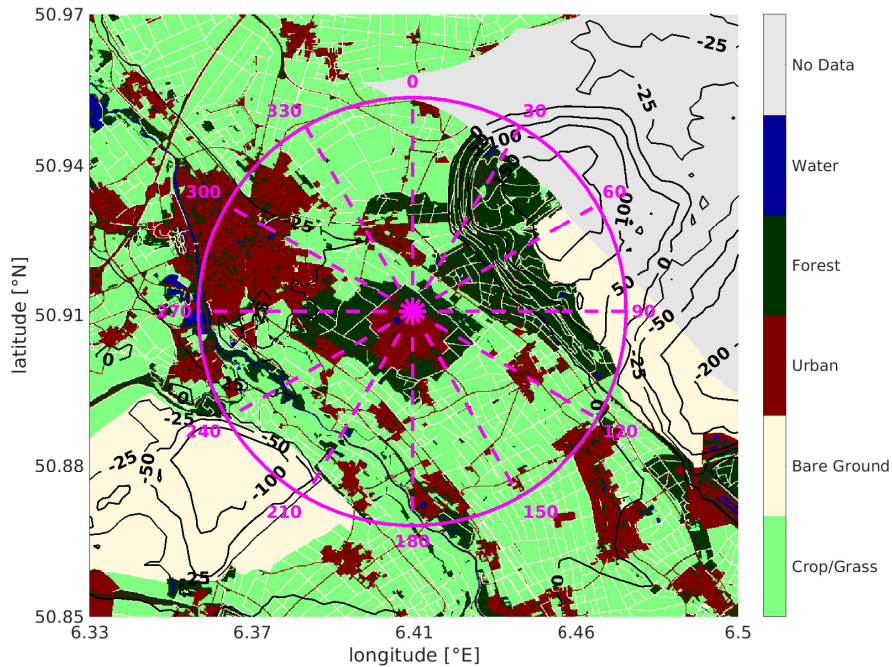
Figure 1. Simplified map (12x13 km) of the land use classification described in Waldhoff et al. (2017) centered around JOYCE. The circle (4.3 km radius) shows the crossing distance and azimuth angles of the MWR scans at the IWV scaling height of 2.5 km. Contours refer to the height relative to JOYCE (111 m a.s.l.).

20 km vertical extent is used in this study. The minimal layer thickness is 20 m and the lowest 2 km contain 33 levels. Initial and lateral boundary conditions are created from the output of the ECMWF Integrated Forecasting System (IFS) model. As the IFS and the ICON model are not using an identical land surface model, a sensitivity of the simulations against the treatment of soil moisture and other land surface components can not be excluded. But those sensitivities are the same for both simulations

5 and sensitivity studies implicate, that the results are rather robust despite small variations. In addition to the control simulation using a simplified version of the land use input data GLOBCOVER (Bontemps et al., 2011) with a 300 m resolution, a second simulation is conducted with an altered land use setting. In this way parameters like leaf area index and roughness length are changed to get a different distribution of potential water vapor sources and sinks at the surface.

2.6 Land use classification and measurement site description

10 To be able to link atmospheric water vapor measurements with land surface properties, spatial land use information is needed. This is addressed by using a remote sensing-based regional crop map (Waldhoff et al., 2017) that was applied to a study area in Western Germany including the surrounding area of JOYCE. In this method, supervised multi-temporal remote sensing

data of Sentinel-2, ancillary information and expert-knowledge on crops are combined in a Multi-Data Approach (MDA). The classification is therefore able to differentiate between 44 vegetated, urban and water areas with a spatial resolution of 15 m.

The detailed and highly resolved classification is used to identify areas with a predominant land use type. Therefore the classified types are condensed into five main types, in particular agricultural areas and grass land, bare ground, urban areas, deciduous forest and water. These five groups are expected to have a significantly different behavior in terms of transpiration and/or evaporation and therefore might cause atmospheric water vapor patterns that can be distinguished and related to the appropriate type. In Fig. 1 the simplified land use classification of a 12x13 km area centered around JOYCE is shown. The city of Jülich to the northwest but also JOYCE at the Research Center Jülich are the largest urban areas in this surrounding. The artificially created pit mine dump hill Sophienhöhe is located in the northeast direction, which is up to 200 m higher than JOYCE and covered mainly by a deciduous forest. In the northern and southeastern part of the selected domain mostly agricultural sites can be identified. The main crop types between April and September are winter wheat and sugar beet, but also maize and potato. A common crop rotation is a two year cycle of sugar beet to winter wheat (Waldhoff et al., 2017). Due to this crop rotation and regarding the small field sizes in this domain, no further distinction in crop types is made. The southwestern parts are mostly grass lands surrounding the Rur River, with its valley going from southeast to northwest. The pit mines (bare ground) with depressions down to 300 m below JOYCE are located to the east and southwest.

3 Long-term observed directional IWV deviations

3.1 Data sample derivation and characteristics

In order to find patterns in the long-term water vapor scans at JOYCE, that can be related to local land surface characteristics, the MWR scans are evaluated during meteorological conditions that are favorable for strong land surface atmosphere inter- actions. This excludes overcast situations and large scale advection of moist or dry air as during these the surface influence is low as shown by Steinke et al. (2019) by the amplitude reduction of the diurnal water vapor cycle. The cloud detection is obtained by using the 31.4 GHz channel, which is within an atmospheric window. The signal from this channel is dominated by the presence of liquid water in case of clouds appearing in the instrument's field of view. During a single scan the maximum difference of the measured 31.4 GHz brightness temperature for each azimuth direction and the mean of the whole scan must be below 2 K, since liquid water clouds are expected to cause a much higher difference. Furthermore the air-mass corrected LWP from the statistical retrieval needs to be below $20\,\mathrm{g\,m^{-2}}$, which is in the order of the retrieval uncertainty. To avoid scenes with large scale advection of moist or dry air, the difference between the maximum and minimum $\mathrm{IWV_z}$ within one hour around the scan needs to be smaller than $2\,\mathrm{kg\,m^{-2}}$, which is above the instrument sensitivity. These requirements need to be fulfilled for at least three consecutive scans. The first and last scan of each sequence is neglected to ensure that they are not part of a transition from conditions violating the criteria. The choice of the thresholds showed to be a good trade-off between excluding apparent cloudy situations, but still allowing a sufficient number of scans to generate a large data sample. Only the months between April and September between 2012–2018 are regarded, since the highest diurnal IWV variability is observed between
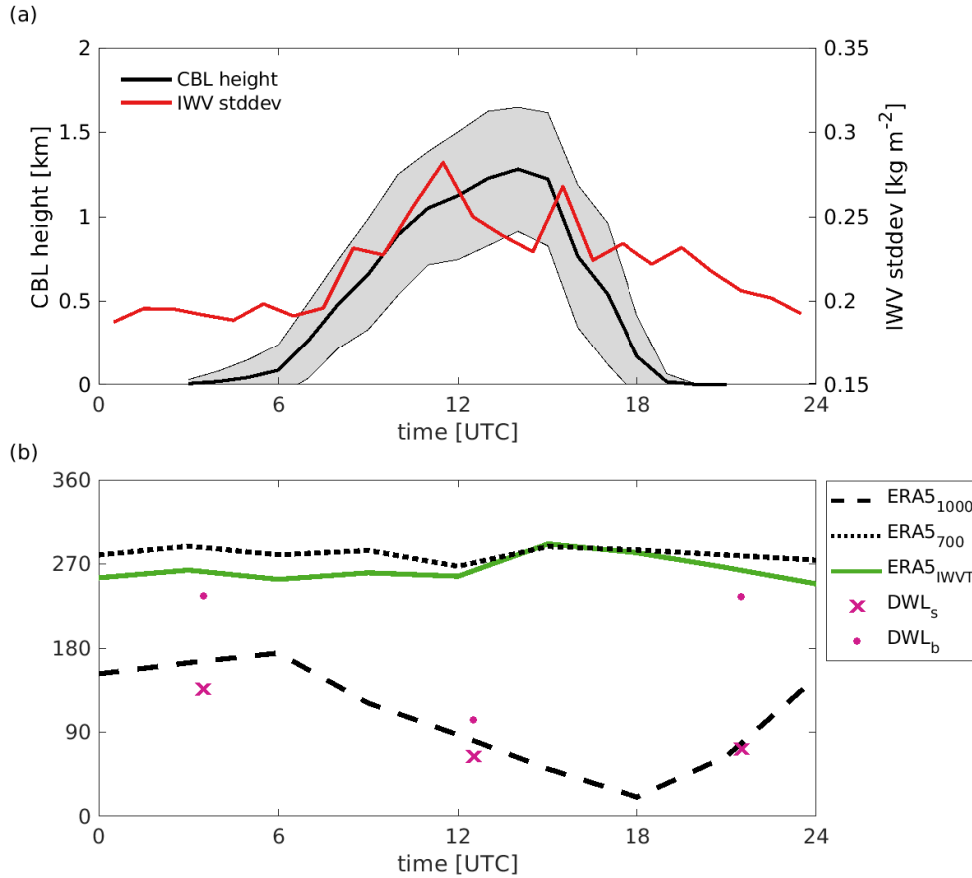
Figure 2. (a) Hourly averaged convective boundary-layer (CBL) height (with standard deviation in shadings) from the Doppler lidar boundary-layer classification at the MWR scan times. The zenith IWV standard deviation (stddev) is determined within 1 h around the scans. (b) The lines show the directions (in degree) of the averaged ERA5 wind directions at 1000 hPa (ERA5$_{1000}$), 700 hPa (ERA5$_{700}$) and the IWV transport (ERA5$_{\mathrm{IWVT}}$). Symbols indicate the mean Doppler lidar wind direction (average times: 01–06 UTC, 10–15 UTC, 19–24 UTC) at 105 m (DWL$_{\mathrm{s}}$) and 1005 m (DWL$_{\mathrm{b}}$).

spring and autumn at JOYCE (Löhnert et al., 2015) and the influence from the land surface is expected to be larger. During the observational period 316 days with in total 7261 single scans are selected with a mean IWV$_{\mathrm{z}}$ of $18.00 \pm 6.37 \ \mathrm{kg \ m^{-2}}$ measured in a 1 h window around the scans. At JOYCE the average year-to-year variability in terms of humidity is rather small, but still a good coverage of relatively dry and wet years is achieved in this study. As an exemplary measure, the mean zenith

5 IWV taken around the selected scans for each year ranges from $15.2 \ \mathrm{kg \ m^{-2}}$ to $19.7 \ \mathrm{kg \ m^{-2}}$. Therefore the variability of the zenith IWV values for the different years (4.1-$7.2 \ \mathrm{kg \ m^{-2}}$) is in the range or higher than changes in the mean value. Instead of using the total slant column IWV, the humidity profile is integrated up to a scaling height of 2.5 km (hereafter: IWV$_{2.5}$) for an

analysis of the lower tropospheric water vapor patterns. This height, where the humidity profile drops below $1/e$, was found by averaging the $1/e$ heights from all zenith measurements of the MWR within 1 h around each of the selected scans. A similar scaling height was also found using satellite data (Simon and Joshi, 1994). For all scans, the mean value per scan is subtracted to investigate the deviations in each azimuth direction.

In addition, a co-located Doppler lidar is used to gain information on atmospheric turbulence, wind direction and wind speed during the scans. The temporal resolution of the Doppler lidar VAD scans is 15 min and the closest measurement to the scan time is selected. For the general development of the wind direction during the day, 6 h averages are calculated. The number of scans per hour that meet the requirements ranges from 127 to 496 with less scans during midday. The decrease in number of
10   cases during daytime is due to the formation of convective clouds, since overcast situations would influence the number of cases independent of the time of the day. The mean standard deviation for each scan increases from 1.1% to 1.94% during daytime indicating the influence of convective activity, which is shown by high TKE dissipation rates and a corresponding mean CBL height up to 1.28 km (Fig. 2(a)). Also the IWV standard deviation from the zenith MWR measurements in Fig. 2(a) reveals a diurnal cycle during this measurement period of late spring until early autumn, which is in agreement with the seasonal
15   statistics derived in Löhnert et al. (2015). While the IWV standard deviation follows the rate of the CBL height development in the morning hours, an abrupt decrease is only evident in the turbulence measurements in the afternoon transition period. This suggests that water vapor is mixed into the upper layers of the atmosphere during daytime and is still present in the residual layer throughout the night.

20   For assessing the impact of the large scale water vapor transport, the ERA5 reanalysis product is used. The ERA5 IWV at the closest output time to the MWR scans compared to the 1 h averaged $\mathrm{IWV_z}$ from the MWR shows a high correlation coefficient of 0.98 and a root-mean-square error (RMSE) of only 1.46 $\mathrm{kg\ m^{-2}}$. The ERA5 wind direction at 1000 hPa ($\mathrm{ERA5_{1000}}$) is in good agreement with the mean near surface wind direction (average times: 01–06 UTC, 10–15 UTC, 19–24 UTC) derived from the Doppler lidar at 105 m ($\mathrm{DWL_s}$, Fig. 2(b)). The wind direction ranges from a southerly flow during night to an east to north
25   direction during the day corresponding to fair weather situations and anticyclonic flow at this site. The wind direction turns clockwise with height for the ERA5 product and the Doppler lidar observations, but stays relatively constant within the CBL as there is no large difference between $\mathrm{DWL_s}$ and the Doppler lidar wind direction at 1005 m ($\mathrm{DWL_b}$) between 10–15 UTC. The wind direction in the free troposphere at 700 hPa shows no significant diurnal cycle. The same applies to the IWVT, that corresponds to the westerly wind direction at 700 hPa, showing the west-wind-zone transport of humid air at the mid-
30   latitudes. But at midday and early afternoon (10–15 UTC) positive $\mathrm{IWV_{2.5}}$ deviations in the long-term MWR scans increase and shift to the southeast (not shown). Despite the fact, that the ERA5 IWV shows a diurnal cycle, this shift can not be seen in the IWVT, suggesting that also local influences contribute to the observed IWV signal. This is further analyzed in section 3.2.

Separating all cases according to the low-level wind direction from the Doppler lidar, a directional dependence is found
35   related to the wind speed. As an example, all MWR scans during northwesterly (270°–360°) winds are averaged separated by
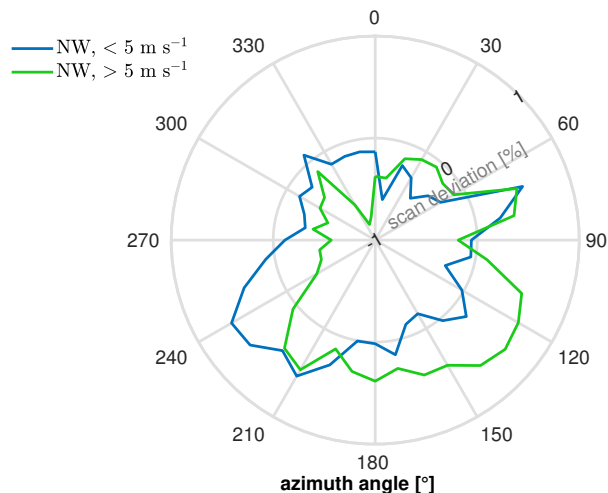
Figure 3. Mean values of the MWR water vapor deviation (integrated up to 2.5 km) from the mean per scan, for all 36 azimuth directions between 10–15 UTC. Different lines indicate MWR scans only for a Doppler lidar determined northwest wind direction and wind speed $< 5 \text{ m s}^{-1}$ (112 scans) and $> 5 \text{ m s}^{-1}$ (74 scans), respectively.

the median wind speed (5 m s^{-1}). Fig. 3 shows the highest positive deviations in the southwest direction for low wind speeds. For higher wind speeds this peak is shifted towards the southeast direction, indicating local transport and a shift of the MWR scanning beam and the underlying surface. The peak around $70°$ is not significantly changing, possibly due to a wind shading effect of the hill to the northeast. This dependency can also be seen for other wind directions. To exclude this process and to

5   better connect the spatial IWV deviations with the surrounding land use, the following analysis is restricted to cases with wind speeds below the median value.

3.2   Daytime MWR and MODIS derived IWV deviations and connection to land use

Figure 4(a) shows the daytime (10–15 UTC) mean value of the $\text{IWV}_{2.5}$ deviation for all 36 azimuth directions. In this time period the highest convective water vapor flux from the land surface into the atmosphere is expected. A positive deviation,

10   as already mentioned for the northwest wind only scans (Fig. 3), up to 0.43% from the mean between 200–$260°$ is visible. Also a positive peak around $75°$ is present. Whereas between $270°$–$60°$ mostly negative $\text{IWV}_{2.5}$ deviations are present (up to -0.32%). Note that these deviations are median values to detect the long-term pattern and that single scan deviations from the mean can get over 5%.

15   For a comparison with an independent IWV measurement and to exclude that the patterns are influenced by interference, the MWR results are compared to the MODIS-NIR derived IWV around JOYCE. The findings presented here could also be valuable for further studies using the MODIS products for assessing spatial IWV differences, which is especially valuable for larger areas. For a fair comparison of the column amount of water vapor from MODIS to the path-integrated water vapor observations
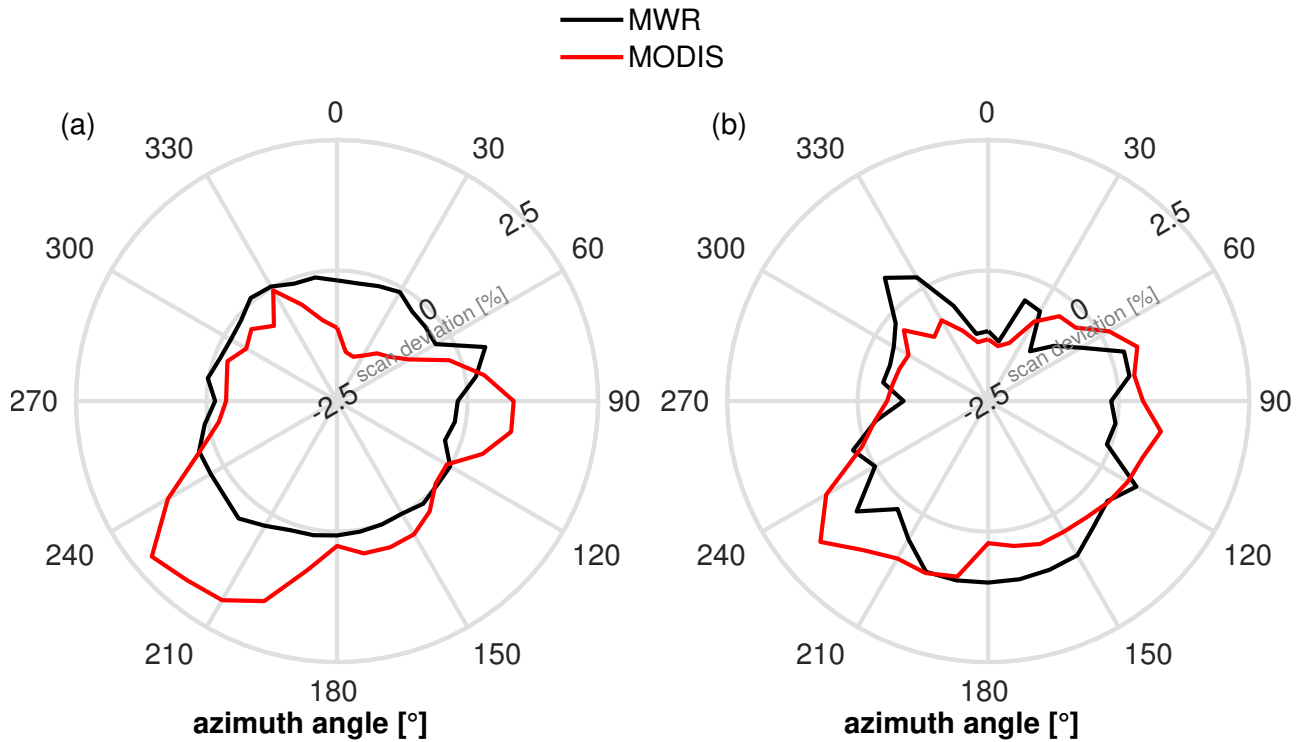
Figure 4. (a) Mean values of the MWR water vapor deviation (integrated up to 2.5 km) from the mean per scan between 10–15 UTC and wind speeds $< 5 \, \mathrm{m \, s^{-1}}$ (406 scans). And mean values of the MODIS IWV deviations including 44 overpasses. (b) Same as (a), but for the 25 July 2012 case study including four MWR scans (10:15–11:10 UTC) and two MODIS overpasses (10:00 UTC, 11:40 UTC).

from the MWR scans, a virtual MWR scan is derived from the MODIS observations. Therefore the total IWV is distributed to an absolute humidity profile for each MODIS pixel assuming a linear decrease by 20% in the CBL and an exponential decrease above similar to Schween et al. (2011). The mean CBL height is determined from the Doppler lidar based boundary-layer classification (Manninen et al., 2018) around 1 h of each overpass. The CBL height is assumed to be constant in the area of interest,

5   as well as the $1/e$ height for the exponential decrease, which is calculated from the MWR humidity profile of the corresponding overpass. In this way a virtual scan corresponding to the MWR scan configuration can be performed around JOYCE where the amount of water vapor is integrated for each beam. Only overpasses without missing data due to the MODIS quality checks are considered. A circular area with a radius of 4.3 km is chosen. This radius corresponds to the distance, where the beam at $30°$ reaches the water vapor scaling height of 2.5 km, which was found on average in the zenith MWR humidity measurements.

As an additional comparison of MWR and MODIS, the $\mathrm{IWV_z}$ measurements of the MWR ($\mathrm{IWV_{z,MWR}}$) and the MODIS mean total column amount 1 km around JOYCE ($\mathrm{IWV_{z,MODIS}}$) are compared. The zenith IWV values are highly correlated (0.99) with a RMSE of 2.93 $\mathrm{kg \, m^{-2}}$, which is about 1 $\mathrm{kg \, m^{-2}}$ higher than found in Steinke et al. (2015). This discrepancy is
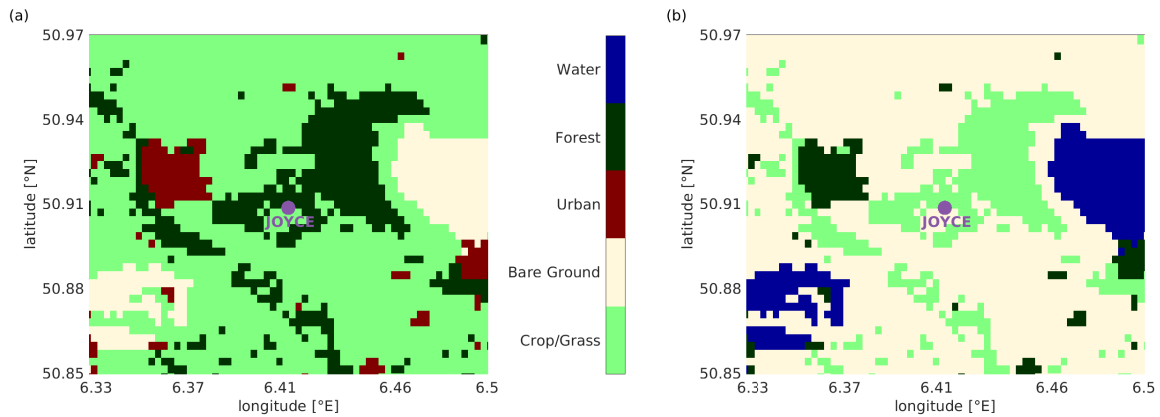
Figure 5. (a) 12x13 km map of the simplified GLOBCOVER land use data centered around JOYCE used for the first ICON-LEM simulation (ICON1). (b) Same as (a) but with altered land use types for the second simulation (ICON2).

probably caused by a greater IWV variability shown in Fig. 2(a). For larger IWV values, the MODIS observations tend to an overestimation. For the 44 MODIS overpasses occurring between 9–13 UTC, the mean IWV deviation from the virtual scans are calculated (Fig. 4(a)). Note that only showing the MWR scans during the MODIS overpasses does not change the deviation pattern significantly.

In general, the relative deviations from the MODIS virtual scans are higher by a factor of about 3–5. With both observations, a noticeable negative deviation between 270°–60° is visible, but also the agreement in the location of the maximum positive deviations around 225° is evident. This area shows a high fraction of crop and grassland, the Rur River and one of the pit mines, whereas less water vapor seems to be present in the vicinity of the urban area and forested hill (Fig. 1). Regarding the MODIS

10 derived results, also the pit mine around 90° reveals a positive deviation, but the peak for the MWR is shifted. This phenomena might be explained by the orographic flow which is strongly altered by the pit mines as shown in Marke et al. (2018) and the low spatial resolution of the MODIS IWV product. The results suggest a higher water vapor flux into the atmosphere for the agricultural fields due to evapotranspiration (no irrigation) and the high amount of water vapor around the pit mines could be caused by irrigation to reduce dust emissions during the day and dew formation at night. In contrast, the forest and urban

15 areas reveal a lower water vapor amount. This can be explained by less water availability in urban areas and a higher water use efficiency for deciduous forests compared to crop fields demonstrated in Tang et al. (2015). A similar difference in the surface fluxes between crops during the main vegetation period and forest (pine trees) was found using surface flux measurements (Beyrich et al., 2006) and in the LES study by Garcia-Carreras et al. (2011). In addition, lower wind speeds due to the topography and a higher roughness length at the forested hill can cause decreased water vapor fluxes into the atmosphere. Thus,

20 spatial water vapor differences can be detected by the scanning MWR, especially in a long-term perspective using a composite of carefully selected cases.
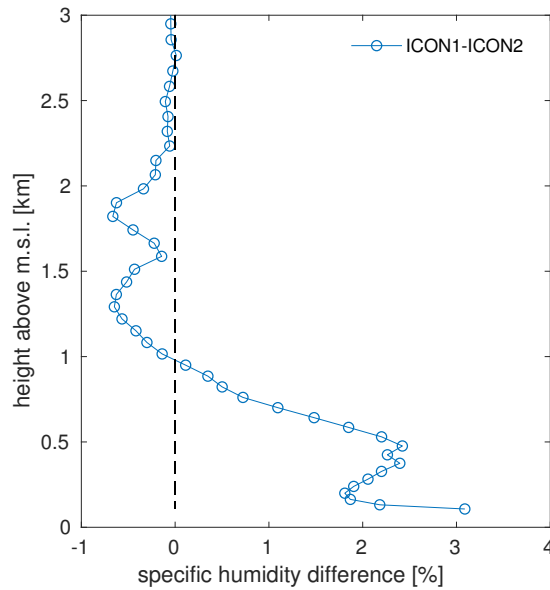
Figure 6. ICON-LEM specific humidity difference (ICON1−ICON2) profile averaged for the domain shown in Fig. 5.

4   LES case study analysis for land surface impact

The influence of the land use type on the evolution of the cloudy boundary-layer is further investigated in a case study (25 July 2012) by means of a large-eddy simulation using the ICON-LEM model. On this day, with a northwesterly wind direction, no clouds are observed until 12:30 UTC and the timings of the MODIS overpasses are 10:00 UTC and 11:40 UTC. In this time interval the CBL height determined by the Doppler lidar increases from 885 m to 1305 m and four MWR scans are performed. The results of the water vapor deviations are shown in Fig. 4(b). As already shown in the previous long-term analysis, the maximum positive deviation occurs in a southwesterly direction (MODIS) with a good agreement in the sign changes between MWR and MODIS. The positive peak for the MWR scans is shifted to the south, which is similar to the higher wind speed cases in Fig. 3, despite observed near surface wind speeds of only around $3\,\mathrm{m\,s^{-1}}$. In order to make a general statement whether the ICON-LEM is correctly representing the spatial water vapor distribution, several high resolution simulations would be needed. Here, the focus is on assessing the impact of different land use data as input for the model on boundary-layer development and cloud formation.

In the first ICON-LEM simulation (ICON1) using the simplified GLOBCOVER land use data (Fig. 5(a)), the model boundary-layer height reaches these heights about one hour later than in the observations. The mean $\mathrm{IWV_z}$ values are $24.83\,\mathrm{kg\,m^{-2}}$ (MWR), $29.26\,\mathrm{kg\,m^{-2}}$ (MODIS) and $28.22\,\mathrm{kg\,m^{-2}}$ (ICON1), where the ICON1 zenith IWV is averaged within a radius of 1 km around JOYCE and for MODIS the nearest pixel is chosen. In a second simulation (ICON2), the land use types are

changed according to Fig. 5(b) (crop/grass to bare ground, bare ground to water, urban to forest, forest to crop/grass and water to urban). In this way, a significant reconstruction in the spatial distribution of the land use types is achieved without changing the scale of heterogeneity and keeping all occurring types. Also the partitioning of turbulent surface fluxes is largely affected by changing crop/grass land to bare soil, but for the whole simulation time the domain averaged sum of latent and sensible

5   heat only differs by around 10 W m^{-2} between ICON1 and ICON2. The maximum height above ground, where changing the land use types has still a significant influence on model parameters, is around 2.3–2.5 km, which is visible for example in the domain averaged specific humidity difference (ICON1−ICON2) profile (Fig. 6). Above this height the large scale forcings are more dominant, which are the same for both simulations. The highest difference occurs in the CBL, which is in agreement with Sühring and Raasch (2013) showing that heterogeneous surface patterns extend throughout the CBL for simulated turbulent

10   heat fluxes. Also Shao et al. (2013) found an influence of land-surface heterogeneity well beyond the surface layer using LES.

In order to elaborate the details of different boundary-layer and cloud development, the spatial fields of height and time averaged vertical velocity and integrated humidity up to 2.5 km ($IWV_{2.5}$) are analyzed (Fig. 7). The averaging domain is the same as shown in Fig. 5 and the averaging time is between 12–13 UTC, which is the time range of the first cloud formation

15   in the simulations. Poll et al. (2017) also performed large-eddy simulations of this day in a similar domain and showed the occurrence of clouds around this time in visible satellite data. They found cellular structures regarding the vertical velocity, which is also evident in Fig. 7(a). In addition, the wind is lifted by the hill and a downdraft above the hill can be seen. This was already discussed in Marke et al. (2018) and might explain parts of the negative scan deviations to the northeast, as discussed in Sect. 3.2, by a suppressed water vapor flux. Moreover the hill serves as a natural border and is impacting by channeling the

20   updraft streak with associated water vapor transport and cloud formation going from northwest to southeast. The streaks are also visible in simulations using a larger domain, lower resolution, no topography and only bare ground (not shown), but the position and strength is strongly altered by the topography and land use input.

In the ICON2 simulation the differences in surface properties and the size of the heterogeneous land use patches intensifies

25   the vertical velocity streak structure, leading to a higher water vapor transport from the surrounding area into the updraft region and an earlier cloud formation. The water bodies introduced in the second simulation show higher $IWV_{2.5}$ values (Fig. 7(d)), but sensible heat flux and CBL height are too low for clouds to form. The mean cloud cover of 8.55% in ICON1 compared to 10.55% in ICON2 is closer to the observed maximum cloud cover of 6% determined by a total sky imager at JOYCE on this day.

30   Less vegetated areas and hence a lower roughness length in ICON2 also lead to an increase in the mean wind speed of 0.42 m s^{-1} at approximately 200 m above ground. With higher wind speeds and a higher fraction of bare ground the domain averaged sensible heat flux (between 11–18 UTC) in ICON2 is increased by 28.72 W m^{-2} and the CBL grows deeper (by about 30 m) especially in the southeastern part of the domain. On the other side the specific humidity in ICON1 is significantly larger in the CBL (Fig. 6) and clouds grow taller compared to the ICON2 simulation (Fig. 8), which is connected to an increased latent

35   heat flux by 86.04 W m^{-2} in ICON1 due to more vegetated areas. Also the maximum integrated cloud water content of these
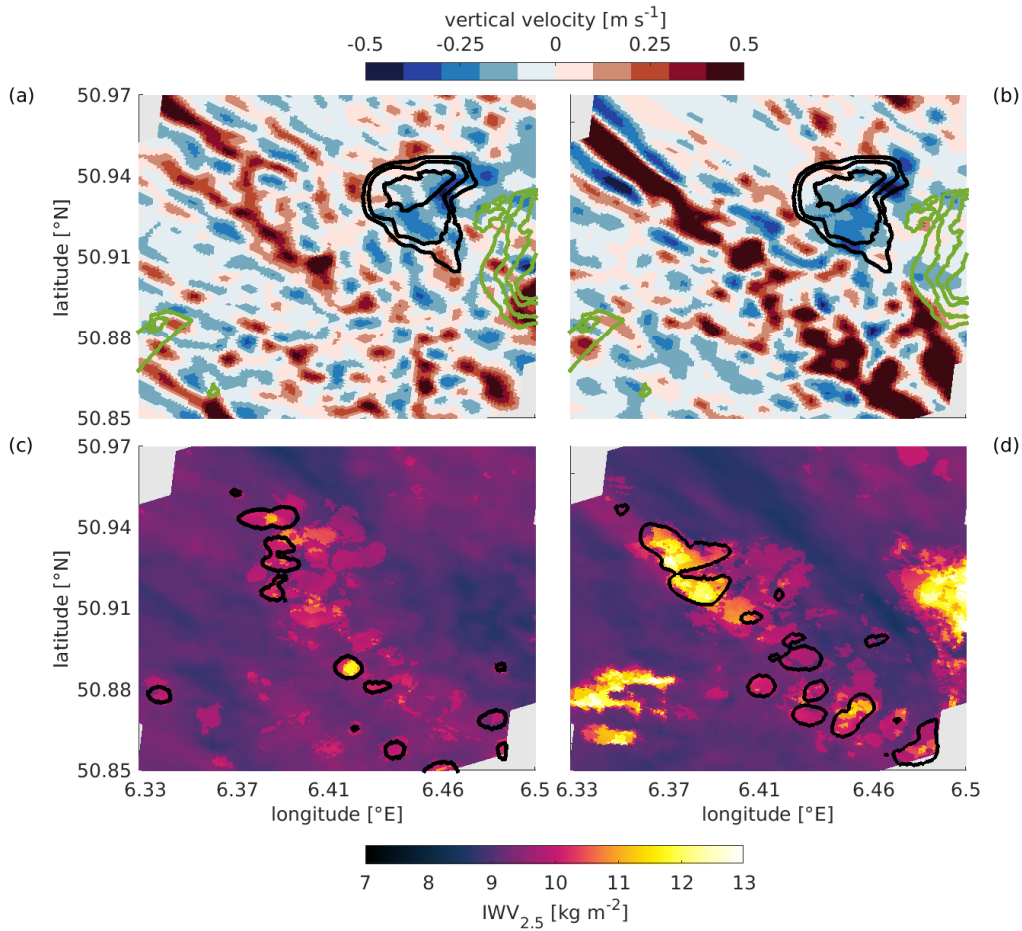
Figure 7. ICON-LEM vertically averaged vertical velocity (top) and integrated humidity (bottom) up to 2.5 km of the ICON1 (a,c) and ICON2 (b,d) simulations. Contours in (a), (b) refer to the topography relative to JOYCE in ma.s.l. between -200 m to 0 m (green) and 0 m to 200 m (black) in 50 m steps. Contours in (c), (d) show areas with total column integrated cloud water values above $10\,\mathrm{g\,m^{-2}}$. The results are averaged between 12–13 UTC.

clouds is $36.96\,\mathrm{g\,m^{-2}}$ (ICON1) and only $5.61\,\mathrm{g\,m^{-2}}$ in ICON2 because of the limited moisture supply. The drastic change in the land use data input for ICON2 therefore causes a shift in the partitioning between sensible and latent heat flux, which has strong implications for the development of convective clouds. Thus the long-term observed spatial water vapor deviations and high-resolution LES conducted in this study underline the importance of further monitoring and modeling the local and small scale interactions between land use, topography, water vapor transport and the transition to clouds.
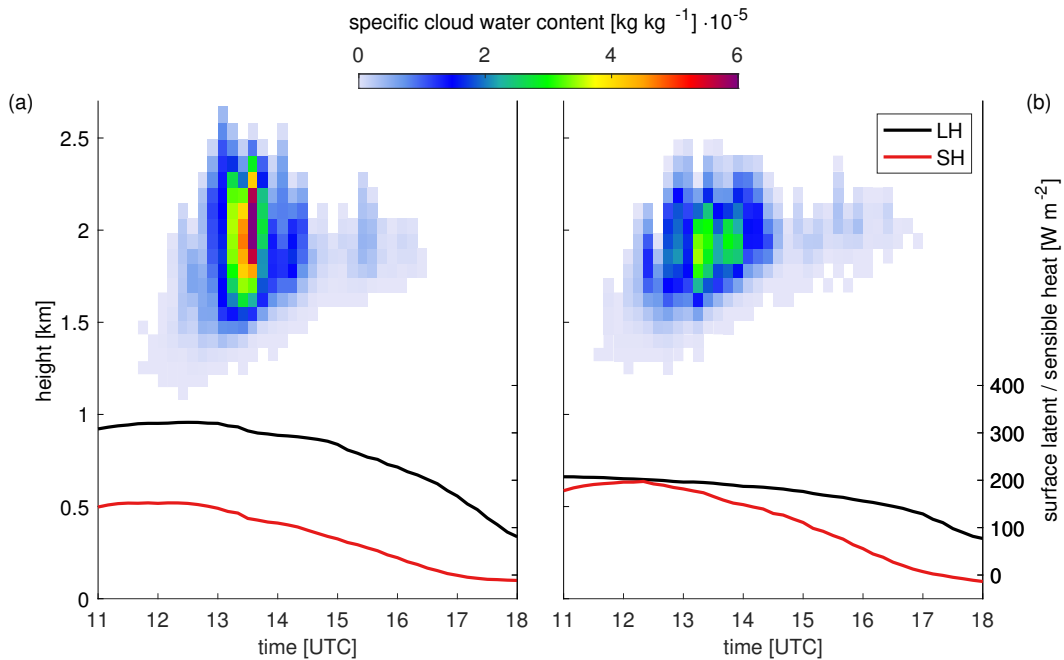
Figure 8. ICON-LEM specific cloud water content for the ICON1 (a) and ICON2 (b) simulation together with the surface fluxes of latent and sensible heat. The results are averaged for the domain shown in Fig. 5.

5   Conclusions

Exchange processes between the land surface and atmosphere are an important controlling factor in the water cycle. Long-term observational evidence of this interaction spanning scales of a few kilometers is still lacking. The scanning microwave radiometer (MWR) at the Jülich ObservatorY for Cloud Evolution (JOYCE) proved to be suitable for detecting spatial IWV deviations for single scans, but also in a statistical sense. The atmospheric water vapor pattern can only partly be explained by the large-scale driven advection and is also attributed to the local transport of water vapor from the surface, especially during convective scenes. This is detected in the the long-term analysis of liquid water cloud free scans within six years of observations.

The comparison to the satellite-based MODIS near-infrared IWV product, as an independent observation, shows similar features of areas with pronounced positive and negative deviations around JOYCE. In a further step, these deviations can be related qualitatively to land surface properties by means of a land use classification. The classification is based on a remote sensing derived regional crop map and reveals, that positive IWV deviations mainly originate over agriculture areas and open pit mines close to the measurement site, while urban and elevated forest areas show negative deviations. The locations of the maximum and minimum deviation in the MODIS and MWR measurements are in agreement.

In a comprehensive case study, large-eddy simulations by the high resolution ICON-LEM model were carried out to further assess the impact of the land surface on the development of the cloudy boundary-layer. While the control simulation is initiated with a realistic land use input, the second simulation with modified land use types revealed changes in convective motions and cloud characteristics according to differences in surface fluxes. These findings suggest that ground-based remote sensing of water vapor supported by high resolution modeling can be valuable for studying the regional influence of heterogeneous land surfaces on the atmospheric water vapor and the connection between surface fluxes, water vapor and clouds.

Author contributions. TM, SC and UL designed the experiments and processed the observational data. VS performed the ICON-LEM simulations and TM prepared the manuscript with contributions from all co-authors.

Competing interests. The authors declare that they have no conflict of interest.

Acknowledgements. The authors would like to acknowledge the Transregional Collaborative Research Centre (TR32) "Patterns in Soil-Vegetation-Atmosphere Systems" funded by the German Science Foundation (DFG), which has continuously contributed to the instrumentation of JOYCE-CF and its maintenance as well as funding T. Marke. Further, the Humidity And Temperature PROfiler (HATPRO) used in this study have been funded by DFG infrastructural programs under the grant INST 216/681-1. The MODIS/Terra Total Precipitable Water Vapor 5-Min L2 Swath 1km dataset was acquired from the Level-1 and Atmosphere Archive & Distribution System (LAADS) Distributed Active Archive Center (DAAC), located in the Goddard Space Flight Center in Greenbelt, Maryland (https://ladsweb.nascom.nasa.gov/).

References

Adler, B., Kalthoff, N., Kohler, M., Handwerker, J., Wieser, A., Corsmeier, U., Kottmeier, C., Lambert, D., and Bock, O.: The variability of water vapour and pre-convective conditions over the mountainous island of Corsica, Quarterly Journal of the Royal Meteorological Society, 142, 335–346, https://doi.org/10.1002/qj.2545, 2016.

5   Avissar, R. and Schmidt, T.: An Evaluation of the Scale at which Ground-Surface Heat Flux Patchiness Affects the Convective Boundary Layer Using Large-Eddy Simulations, Journal of the Atmospheric Sciences, 55, 2666–2689, https://doi.org/10.1175/1520-0469(1998)055<2666:aeotsa>2.0.co;2, 1998.

Beyrich, F., Leps, J.-P., Mauder, M., Bange, J., Foken, T., Huneke, S., Lohse, H., Lüdi, A., Meijninger, W. M. L., Mironov, D., Weisensee, U., and Zittel, P.: Area-Averaged Surface Fluxes Over the Litfass Region Based on Eddy-Covariance Measurements, Boundary-Layer

10   Meteorology, 121, 33–65, https://doi.org/10.1007/s10546-006-9052-x, 2006.

Bontemps, S., Defourny, P., Van Bogaert, E., Arino, O., Kalogirou, V., and Ramos Perez, J. J.: GLOBCOVER 2009 Products Description and Validation Report, Université catholique de Louvain (UCL) & European Space Agency (ESA), 2.2, 53 pp, 2011.

Clark, C. A. and Arritt, P. W.: Numerical Simulations of the Effect of Soil Moisture and Vegetation Cover on the Development of Deep Convection, Journal of Applied Meteorology, 34, 2029–2045, https://doi.org/10.1175/1520-0450(1995)034<2029:NSOTEO>2.0.CO;2,

15   1995.

Copernicus Climate Change Service (C3S): ERA5: Fifth generation of ECMWF atmospheric reanalyses of the global climate. Copernicus Climate Change Service Climate Data Store (CDS), Copernicus Climate Change Service Climate Data Store (CDS), date of access: 03/03/2019, 2017.

Courault, D., Drobinski, P., Brunet, Y., Lacarrere, P., and Talbot, C.: Impact of surface heterogeneity on a buoyancy-driven convective

20   boundary layer in light winds, Boundary-Layer Meteorology, 124, 383–403, https://doi.org/10.1007/s10546-007-9172-y, 2007.

Gao, B.-C. and Kaufman, Y. J.: Water vapor retrievals using Moderate Resolution Imaging Spectroradiometer (MODIS) near-infrared channels, Journal of Geophysical Research: Atmospheres, 108, https://doi.org/10.1029/2002jd003023, 2003.

Garcia-Carreras, L., Parker, D. J., and Marsham, J. H.: What is the Mechanism for the Modification of Convective Cloud Distributions by Land Surface–Induced Flows?, Journal of the Atmospheric Sciences, 68, 619–634, https://doi.org/10.1175/2010jas3604.1, 2011.

25   Heinze, R., Dipankar, A., Henken, C. C., Moseley, C., Sourdeval, O., Trömel, S., Xie, X., Adamidis, P., Ament, F., Baars, H., Barthlott, C., Behrendt, A., Blahak, U., Bley, S., Brdar, S., Brueck, M., Crewell, S., Deneke, H., Di Girolamo, P., Evaristo, R., Fischer, J., Frank, C., Friederichs, P., Göcke, T., Gorges, K., Hande, L., Hanke, M., Hansen, A., Hege, H.-C., Hoose, C., Jahns, T., Kalthoff, N., Klocke, D., Kneifel, S., Knippertz, P., Kuhn, A., van Laar, T., Macke, A., Maurer, V., Mayer, B., Meyer, C. I., Muppa, S. K., Neggers, R. A. J., Orlandi, E., Pantillon, F., Pospichal, B., Röber, N., Scheck, L., Seifert, A., Seifert, P., Senf, F., Siligam, P., Simmer, C., Steinke, S., Stevens,

30   B., Wapler, K., Weniger, M., Wulfmeyer, V., Zängl, G., Zhang, D., and Quaas, J.: Large-eddy simulations over Germany using ICON: a comprehensive evaluation: Evaluation of ICON in Realistic LES Configuration, Quarterly Journal of the Royal Meteorological Society, 143, 69–100, https://doi.org/10.1002/qj.2947, 2017.

Huang, H. Y. and Margulis, S. A.: On the impact of surface heterogeneity on a realistic convective boundary layer, Water Resources Research, 45, https://doi.org/10.1029/2008WR007175, 2009.

35   Kneifel, S., Crewell, S., Lohnert, U., and Schween, J.: Investigating Water Vapor Variability by Ground-Based Microwave Radiometry: Evaluation Using Airborne Observations, IEEE Geoscience and Remote Sensing Letters, 6, 157–161, https://doi.org/10.1109/LGRS.2008.2007659, 2009.

Löhnert, U. and Crewell, S.: Accuracy of cloud liquid water path from ground-based microwave radiometry 1. Dependency on cloud model statistics, Radio Science, 38, https://doi.org/10.1029/2002rs002654, 2003.

Löhnert, U., Schween, J. H., Acquistapace, C., Ebell, K., Maahn, M., Barrera-Verdejo, M., Hirsikko, A., Bohn, B., Knaps, A., O'Connor, E., Simmer, C., Wahner, A., and Crewell, S.: JOYCE: Jülich Observatory for Cloud Evolution, Bulletin of the American Meteorological Society, 96, 1157–1174, https://doi.org/10.1175/BAMS-D-14-00105.1, https://doi.org/10.1175/BAMS-D-14-00105.1, 2015.

Macke, A., Seifert, P., Baars, H., Barthlott, C., Beekmans, C., Behrendt, A., Bohn, B., Brueck, M., Bühl, J., Crewell, S., Damian, T., Deneke, H., Düsing, S., Foth, A., Di Girolamo, P., Hammann, E., Heinze, R., Hirsikko, A., Kalisch, J., Kalthoff, N., Kinne, S., Kohler, M., Löhnert, U., Madhavan, B. L., Maurer, V., Muppa, S. K., Schween, J., Serikov, I., Siebert, H., Simmer, C., Späth, F., Steinke, S., Träumner, K., Trömel, S., Wehner, B., Wieser, A., Wulfmeyer, V., and Xie, X.: The {HD}({CP})² {Observational} {Prototype} {Experiment} ({HOPE}) – an overview, Atmospheric Chemistry and Physics, 17, 4887–4914, https://doi.org/10.5194/acp-17-4887-2017, 2017.

Manninen, A. J., Marke, T., Tuononen, M., and O'Connor, E. J.: Atmospheric Boundary Layer Classification With Doppler Lidar, Journal of Geophysical Research: Atmospheres, 123, 8172–8189, https://doi.org/10.1029/2017JD028169, 2018.

Marke, T., Crewell, S., Schemann, V., Schween, J. H., and Tuononen, M.: Long-term observations and high-resolution modeling of midlatitude nocturnal boundary layer processes connected to low-level jets, Journal of Applied Meteorology and Climatology, 57, 1155–1170, https://doi.org/10.1175/JAMC-D-17-0341.1, 2018.

Maronga, B. and Raasch, S.: Large-Eddy Simulations of Surface Heterogeneity Effects on the Convective Boundary Layer During the LITFASS-2003 Experiment, Boundary-Layer Meteorology, 146, 17–44, https://doi.org/10.1007/s10546-012-9748-z, 2013.

Maschwitz, G., Löhnert, U., Crewell, S., Rose, T., and Turner, D. D.: Investigation of ground-based microwave radiometer calibration techniques at 530 hPa, Atmospheric Measurement Techniques, 6, 2641–2658, https://doi.org/10.5194/amt-6-2641-2013, 2013.

O'Connor, E. J., Illingworth, A. J., Brooks, I. M., Westbrook, C. D., Hogan, R. J., Davies, F., Brooks, and J., B.: A method for estimating the turbulent kinetic energy dissipation rate from a vertically pointing doppler lidar, and independent evaluation from balloon-borne in situ measurements, Journal of Atmospheric and Oceanic Technology, 27, 1652–1664, https://doi.org/10.1175/2010JTECHA1455.1, 2010.

Ookouchi, Y., Segal, M., Kessler, R. C., and Pielke, R. A.: Evaluation of Soil Moisture Effects on the Generation and Modification of Mesoscale Circulations, Monthly Weather Review, 112, 2281–2292, https://doi.org/10.1175/1520-0493(1984)112<2281:eosmeo>2.0.co;2, 1984.

Pearson, G., Davies, F., and Collier, C.: An Analysis of the Performance of the UFAM Pulsed Doppler Lidar for Observing the Boundary Layer, Journal of Atmospheric and Oceanic Technology, 26, 240–250, https://doi.org/10.1175/2008JTECHA1128.1, 2009.

Pielke, R. A., Dalu, G. A., Snook, J. S., Lee, T. J., and Kittel, T. G. F.: Nonlinear Influence of Mesoscale Land Use on Weather and Climate, Journal of Climate, 4, 1053–1069, https://doi.org/10.1175/1520-0442(1991)004<1053:niomlu>2.0.co;2, 1991.

Poll, S., Shrestha, P., and Simmer, C.: Modelling convectively induced secondary circulations in the *terra incognita* with TerrSysMP: Modelling CISCs in the Terra Incognita with TerrSysMP, Quarterly Journal of the Royal Meteorological Society, 143, 2352–2361, https://doi.org/10.1002/qj.3088, 2017.

Rabin, R. M., Stadler, S., Wetzel, P. J., Stensrud, D. J., and Gregory, M.: Observed Effects of Landscape Variability on Convective Clouds, Bulletin of the American Meteorological Society, 71, 272–280, https://doi.org/10.1175/1520-0477(1990)071<0272:oeolvo>2.0.co;2, 1990.

Rose, T., Crewell, S., Löhnert, U., and Simmer, C.: A network suitable microwave radiometer for operational monitoring of the cloudy atmosphere, Atmospheric Research, 75, 183–200, https://doi.org/10.1016/j.atmosres.2004.12.005, 2005.

Schween, J. H., Crewell, S., and Löhnert, U.: Horizontal-humidity gradient from one single-scanning microwave radiometer, IEEE Geoscience and Remote Sensing Letters, 8, 336–340, https://doi.org/10.1109/LGRS.2010.2072981, 2011.

Shao, Y., Liu, S., Schween, J. H., and Crewell, S.: Large-Eddy Atmosphere–Land-Surface Modelling over Heterogeneous Surfaces: Model Development and Comparison with Measurements, Boundary-Layer Meteorology, 148, 333–356, https://doi.org/10.1007/s10546-013-9823-0, 2013.

Simmer, C., Thiele-Eich, I., Masbou, M., Amelung, W., Bogena, H., Crewell, S., Diekkrüger, B., Ewert, F., Hendricks Franssen, H.-J., Huisman, J. A., Kemna, A., Klitzsch, N., Kollet, S., Langensiepen, M., Löhnert, U., Rahman, A. S. M. M., Rascher, U., Schneider, K., Schween, J., Shao, Y., Shrestha, P., Stiebler, M., Sulis, M., Vanderborght, J., Vereecken, H., van der Kruk, J., Waldhoff, G., and Zerenner, T.: Monitoring and Modeling the Terrestrial System from Pores to Catchments: The Transregional Collaborative Research Center on Patterns in the Soil–Vegetation–Atmosphere System, Bulletin of the American Meteorological Society, 96, 1765–1787, https://doi.org/10.1175/BAMS-D-13-00134.1, 2015.

Simon, B. and Joshi, P. C.: Determination of moisture changes prior to the onset of south-west monsoon over Kerala using NOAA/TOVS satellite data, Meteorology and Atmospheric Physics, 53, 223–231, https://doi.org/10.1007/BF01029613, 1994.

Späth, F., Behrendt, A., Kumar Muppa, S., Metzendorf, S., Riede, A., and Wulfmeyer, V.: 3-D water vapor field in the atmospheric boundary layer observed with scanning differential absorption lidar, Atmospheric Measurement Techniques, 9, 1701–1720, https://doi.org/10.5194/amt-9-1701-2016, 2016.

Steinke, S., Eikenberg, S., Löhnert, U., Dick, G., Klocke, D., Di Girolamo, P., and Crewell, S.: Assessment of small-scale integrated water vapour variability during HOPE, Atmospheric Chemistry and Physics, 15, 2675–2692, https://doi.org/10.5194/acp-15-2675-2015, 2015.

Steinke, S., Wahl, S., and Crewell, S.: Benefit of high resolution COSMO reanalysis: The diurnal cycle of column-integrated water vapor over Germany, Meteorologische Zeitschrift, 28, 165–177, https://doi.org/10.1127/metz/2019/0936, 2019.

Sühring, M. and Raasch, S.: Heterogeneity-Induced Heat-Flux Patterns in the Convective Boundary Layer: Can they be Detected from Observations and is There a Blending Height?—A Large-Eddy Simulation Study for the LITFASS-2003 Experiment, Boundary-Layer Meteorology, 148, 309–331, https://doi.org/10.1007/s10546-013-9822-1, 2013.

Tang, X., Li, H., Desai, A. R., Nagy, Z., Luo, J., Kolb, T. E., Olioso, A., Xu, X., Yao, L., Kutsch, W., Pilegaard, K., Köstner, B., and Ammann, C.: How is water-use efficiency of terrestrial ecosystems distributed and changing on Earth?, Scientific Reports, 4, https://doi.org/10.1038/srep07483, 2015.

van Heerwaarden, C. C. and Vilà-Guerau De Arellano, J.: Relative Humidity as an Indicator for Cloud Formation over Heterogeneous Land Surfaces, Journal of the Atmospheric Sciences, 65, 3263–3277, https://doi.org/10.1175/2008JAS2591.1, 2008.

Vilà-Guerau De Arellano, J., Ouwersloot, H. G., Baldocchi, D., and Jacobs, C. M.: Shallow cumulus rooted in photosynthesis, Geophysical Research Letters, 41, 1796–1802, https://doi.org/10.1002/2014GL059279, 2014.

Waldhoff, G., Lussem, U., and Bareth, G.: Multi-Data Approach for remote sensing-based regional crop rotation mapping: A case study for the Rur catchment, Germany, International Journal of Applied Earth Observation and Geoinformation, 61, 55–69, https://doi.org/10.1016/j.jag.2017.04.009, 2017.

Weckwerth, T. M., Parsons, D. B., Koch, S. E., Moore, J. A., LeMone, M. A., Demoz, B. B., Flamant, C., Geerts, B., Wang, J., and Feltz, W. F.: An Overview of the International H_2O Project (IHOP_2002) and Some Preliminary Highlights, Bulletin of the American Meteorological Society, 85, 253–278, https://doi.org/10.1175/BAMS-85-2-253, 2004.

Wulfmeyer, V., Behrendt, A., Kottmeier, C., Corsmeier, U., Barthlott, C., Craig, G. C., Hagen, M., Althausen, D., Aoshima, F., Arpagaus, M., Bauer, H.-S., Bennett, L., Blyth, A., Brandau, C., Champollion, C., Crewell, S., Dick, G., Di Girolamo, P., Dorninger, M., Dufournet, Y.,

Eigenmann, R., Engelmann, R., Flamant, C., Foken, T., Gorgas, T., Grzeschik, M., Handwerker, J., Hauck, C., Höller, H., Junkermann, W., Kalthoff, N., Kiemle, C., Klink, S., König, M., Krauss, L., Long, C. N., Madonna, F., Mobbs, S., Neininger, B., Pal, S., Peters, G., Pigeon, G., Richard, E., Rotach, M. W., Russchenberg, H., Schwitalla, T., Smith, V., Steinacker, R., Trentmann, J., Turner, D. D., van Baelen, J., Vogt, S., Volkert, H., Weckwerth, T., Wernli, H., Wieser, A., and Wirth, M.: The Convective and Orographically-induced Precipitation Study (COPS): the scientific strategy, the field phase, and research highlights, Quarterly Journal of the Royal Meteorological Society, 137, 3–30, https://doi.org/10.1002/qj.752, 2011.

Wulfmeyer, V., Turner, D. D., Baker, B., Banta, R., Behrendt, A., Bonin, T., Brewer, W. A., Buban, M., Choukulkar, A., Dumas, E., Hardesty, R. M., Heus, T., Ingwersen, J., Lange, D., Lee, T. R., Metzendorf, S., Muppa, S. K., Meyers, T., Newsom, R., Osman, M., Raasch, S., Santanello, J., Senff, C., Späth, F., Wagner, T., and Weckwerth, T.: A New Research Approach for Observing and Characterizing Land-Atmosphere Feedback, Bulletin of the American Meteorological Society, 99, 1639–1667, https://doi.org/10.1175/BAMS-D-17-0009.1, 2018.

Zängl, G., Reinert, D., Rípodas, P., and Baldauf, M.: The ICON (ICOsahedral Non-hydrostatic) modelling framework of DWD and MPI-M: Description of the non-hydrostatic dynamical core, Quarterly Journal of the Royal Meteorological Society, 141, 563–579, https://doi.org/10.1002/qj.2378, 2015.